

## **Title**

Manifold-based transformation of the probability distribution for convergence in optimization

Tomotaka Oroguchi<sup>1,2\*</sup>, Rintaro Inoue<sup>3</sup>, and Masaaki Sugiyama<sup>3</sup>

<sup>1</sup>Department of Physics, Faculty of Science and Technology, Keio University, 3-14-1 Hiyoshi, Kohoku-ku, Yokohama 223-8522, Japan.

<sup>2</sup>RIKEN SPring-8 Center, 1-1-1 Kouto, Sayo-cho, Sayo-gun, Hyogo 679-5148, Japan

<sup>3</sup>Institute for Integrated Radiation and Nuclear Science, Kyoto University, Kumatori, Sennan-gun, Osaka 590-0494, Japan.

\*Corresponding author

oroguchi@phys.keio.ac.jp

## **Abstract**

Reconstructing probability distributions from experimental data is a crucial problem across various fields. An effective approach is to optimize a theoretical or computational model of the distribution under an objective functional that evaluates consistency with the experimental data. However, achieving convergence in optimization remains a challenge. Given the manifold structure of the probability distribution space, we demonstrate that transformation of distribution in optimization should be infinitesimal displacements along exponential geodesics. Our theory was validated through the reconstruction of protein conformational ensembles, showing its broad applicability.

## Introduction

This study addresses the problem of reconstructing probability distribution from observed data, a fundamental challenge that spans various disciplines, such as physics [1-5], climate science [6,7], engineering [8,9], and machine learning [10,11]. Many systems in these fields have internal distributions that can be represented as probability distributions, such as electronic structures, protein conformational ensembles, and so on. Visualizing these internal distributions is crucial for comprehending system properties, yet it poses significant challenges because, in general, direct observations of the distributions are unavailable through experiments. Experiments typically provide access to distributions only through indirect observables such as spectral data; therefore, it is necessary to reconstruct the distributions from the observables. This reconstruction problem represents an active area of research [12,13]. The most effective approach for such an inverse problem involves optimizing a theoretically or computationally model of the distribution to be consistent with experimental data for observables.

The aforementioned optimization is formulated as a following task for a discretized system comprising  $n$  states, which is a ubiquitous system in physics. By expressing a model probability distribution as  $\mathbf{p} = (p_1, \dots, p_n)$  with the normalization condition  $\sum_{i=1}^n p_i = 1$ , an initial model distribution as  $\mathbf{p}^0$ , observables as  $\mathbf{Y} = (y_1, \dots, y_m)$  with  $m$  data points, experimental data for  $\mathbf{Y}$  as  $\mathbf{Y}^{\text{EXP}}$ ,  $\mathbf{Y}$  calculated from  $\mathbf{p}$  as  $\mathbf{Y}(\mathbf{p})$ , and an objective functional as  $\Phi(\mathbf{Y}(\mathbf{p})||\mathbf{Y}^{\text{EXP}})$ , the task is to optimize  $\mathbf{p}^0$  by minimizing  $\Phi$ . The objective functional  $\Phi(\mathbf{Y}(\mathbf{p})||\mathbf{Y}^{\text{EXP}})$  evaluates the consistency between the model and experimental data (designated as  $\Phi(\mathbf{p})$  hereinafter).

In general, minimizing the objective function necessitates assuming a potential function property [14]. Here, let us consider minimizing the objective function  $\Phi(\xi)$  in Euclidean space  $\xi$ . Then,  $\Phi(\xi)$  can be minimized through iterative transformation of  $\xi$  from the initial position  $\xi^0$  under the gradient field  $\nabla_{\xi}\Phi(\xi)$ . A representative for such transformation is gradient descent expressed as follows:

$$\Delta\xi = -\tau\nabla_{\xi}\Phi(\xi) \tag{1}$$

where  $\Delta\xi$  and  $\tau$  denote the transformation displacement and rate, respectively. Analogous to the

optimization in Euclidean space, many studies on probability distribution optimization [15-17] conduct iterative transformation of  $\mathbf{p}$  from  $\mathbf{p}^0$  under the gradient field  $\nabla_{\mathbf{p}}\Phi(\mathbf{p})$  in probability distribution space  $\mathbf{p}$  (designated as  $\mathbf{p}$ -space hereinafter) (Fig. 1(a)), that is  $\Delta\mathbf{p} \propto -\tau\nabla_{\mathbf{p}}\Phi(\mathbf{p})$ . However, such transformation is feasible only when the  $\mathbf{p}$ -space is Euclidean. Notably, the  $\mathbf{p}$ -space is an  $n-1$  dimensional manifold  $S_{n-1}$ , where the metric tensor is not an identity matrix and varies depending on  $\mathbf{p}$  [18]. Therefore, the gradient should be calibrated by the metric tensor [19], and the transformation under the uncalibrated gradient field  $\nabla_{\mathbf{p}}\Phi(\mathbf{p})$  compromises the potential function property of  $\Phi$ , resulting in optimization divergence [17]. To prevent the divergence, the constraints on the initially modeled distribution  $\mathbf{p}^0$  are often introduced into  $\Phi$  using the framework of maximum entropy [15,16] or Bayesian inference [17,20].

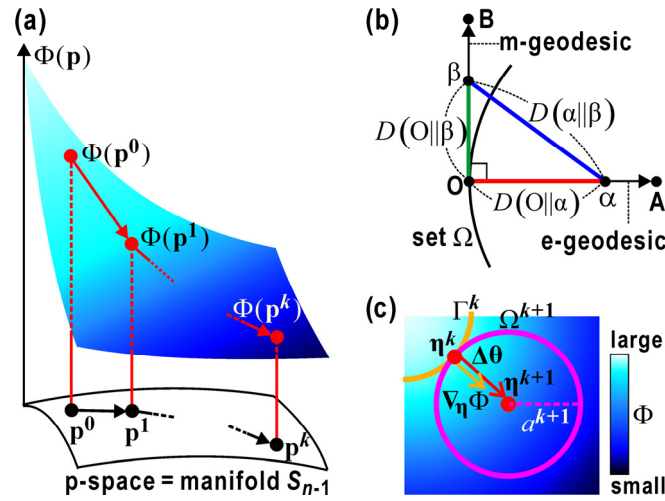


**FIG. 1.** Schematic of the optimization problem of probability distribution  $\mathbf{p}$ . (a) Iterative transformation of  $\mathbf{p}$  from  $\mathbf{p}^0$  under an objective (potential) functional  $\Phi(\mathbf{p})$ . (b) Geometry of the transformation path from point O to A in the  $\mathbf{p}$ -space. (c) Geometry of the transformation of gradient descent in the  $\mathbf{p}$ -space.

In the case of a general Riemannian manifold  $\zeta$  with the metric tensor  $\mathbf{G}(\zeta)$ , the gradient can be calibrated as  $\mathbf{G}^{-1}(\zeta)\nabla_{\zeta}\Phi(\zeta)$ , which is called a natural gradient [19]. However, applying the natural

gradient to the  $\mathbf{p}$ -space remains challenging owing to the unknown normalization constant [21]. As an alternative approach for the  $\mathbf{p}$ -space, we consider the path between two points, which approximately satisfies the geometric conditions of general Euclidean space, namely affine and metric [22]. Then, by applying the principles of the gradient descent in general Euclidean space to this approximate Euclidean path, we formulated the gradient descent in  $\mathbf{p}$ -space with the normalization constant  $C$ , expressed as follows:

$$\Delta \log \mathbf{p} = -\tau \nabla_{\mathbf{p}} \Phi(\mathbf{p}) + C, \quad (2)$$

where  $\log \mathbf{p} = (\log p_1, \dots, \log p_n)$  and  $C = -\log \left( \sum_{i=1}^n p_i \exp(-\tau \partial \Phi / \partial p_i) \right)$ . In the context of information geometry [18], the left-hand side of Eq. (2) corresponds to an infinitesimal change along an exponential geodesic (denoted as e-geodesic hereinafter). The e-geodesic is an affine line, and the Kullback–Leibler (KL) divergence for any infinitesimal change on this line acts as a distance metric. Therefore, the transformation path depicted in Eq. (2) satisfies the conditions of Euclidean space. In this study, we first prove Eq. (2) using information geometry. Subsequently, through numerical simulations, in which protein conformational ensembles are reconstructed from small-angle X-ray scattering (SAXS) data, we demonstrate that optimization based on Eq. (2) achieves excellent convergence.

### **Proof of Eq. (2)**

Here, we define two nearby points  $O$  and  $A$  in the  $\mathbf{p}$ -space (or on the manifold  $S_{n-1}$ ), and consider the transformation from  $\mathbf{p}^O$  and  $\mathbf{p}^A$  (Fig. 1b). The superscripts represent the points on the manifold hereinafter. Our primary objective is to identify a local coordinate system and transformation path that satisfy the geometric conditions of Euclidean space.

(i) An affine coordinate system can be established.

(ii) For any point  $\alpha$  on the path, the distance from point  $O$ ,  $d(O \parallel \alpha)$ , can be defined, satisfying the following conditions:

(ii-a) Positivity and symmetry:  $d(\mathbf{O} \parallel \alpha) = d(\alpha \parallel \mathbf{O}) \geq 0$ .

(ii-b) Pythagorean theorem:  $d(\mathbf{O} \parallel \alpha) + d(\mathbf{O} \parallel \beta) = d(\alpha \parallel \beta)$ .

(ii-c) Triangle inequality:  $\sqrt{d(\mathbf{O} \parallel \alpha)} + \sqrt{d(\mathbf{O} \parallel \beta)} \geq \sqrt{d(\alpha \parallel \beta)}$ .

Information geometry reveals that the manifold  $S_{n-1}$  is a dually flat space [23,24], characterized by the Fisher information metric [25,26]:

$$\mathbf{g}_n \left( \frac{\partial}{\partial \mu_j}, \frac{\partial}{\partial \mu_k} \right) = \sum_{i=1}^n p_i \left( \frac{\partial}{\partial \mu_j} \log p_i \right) \left( \frac{\partial}{\partial \mu_k} \log p_i \right). \quad (3)$$

where  $\partial/\partial \mu_j$  denotes the tangent vector regarding the local coordinate system  $\boldsymbol{\mu}$ . In the dually flat manifold, mutually dual affine coordinate systems exist [19,23,24],  $\boldsymbol{\theta} = (\theta_1, \dots, \theta_{n-1})$  and  $\boldsymbol{\eta} = (\eta_1, \dots, \eta_{n-1})$ , expressed as follows:

$$\theta_i = \log(p_i/p_n) \quad \text{and} \quad \eta_i = p_i. \quad (4)$$

$\boldsymbol{\theta}$  and  $\boldsymbol{\eta}$  are called exponential-connection (e-connection) and mixture-connection (m-connection) coordinate systems, respectively. In these coordinate systems, the Fisher information metric becomes

$$\mathbf{g}_n \left( \frac{\partial}{\partial \theta_i}, \frac{\partial}{\partial \eta_j} \right) = \delta_{ij}. \quad (5)$$

Since only  $\boldsymbol{\theta}$  and  $\boldsymbol{\eta}$  are dual affine coordinate systems on  $S_{n-1}$ , the use of either of them is necessary for Euclidean space condition (i). Here,  $\boldsymbol{\eta}$  is selected as a coordinate system, leading to the introduction of the KL divergence [27-29] defined as follows:

$$D(\mathbf{O} \parallel \alpha) = \sum_{i=1}^n p_i^{\mathbf{O}} \log \frac{p_i^{\mathbf{O}}}{p_i^{\alpha}}, \quad (6)$$

for the two points,  $\mathbf{O}$  and  $\alpha$ .  $D$  is non-negative and quantifies the difference between the two distributions  $\mathbf{p}^{\mathbf{O}}$  and  $\mathbf{p}^{\alpha}$ .

Here, we assume that point  $\alpha$  lies on the e-geodesic [30] connecting points  $\mathbf{O}$  and  $\mathbf{A}$  (Fig. 1(b)). Since the e-geodesic is an affine line with respect to  $\boldsymbol{\theta}$ , point  $\alpha$  and tangent vector  $\mathbf{v}$  along this line can be expressed as

$$\theta_i^\alpha = \theta_i^O + s(\theta_i^A - \theta_i^O) \quad (0 \leq s \leq 1) \quad \text{and} \quad \mathbf{v} = \sum_{i=1}^{n-1} (\theta_i^A - \theta_i^O) \frac{\partial}{\partial \theta_i}, \quad (7)$$

respectively. For Euclidean space condition (i), the transformation along an e-geodesic is imperative. Additionally, we consider the displacement from O to A,  $\Delta \mathbf{p}^A = \mathbf{p}^A - \mathbf{p}^O$ , to be infinitesimal, enabling us to disregard third or higher-order terms. Consequently, for any point  $\alpha$  on the e-geodesic between O and A, the KL divergence,  $D(O \parallel \alpha)$ , approximately functions as a distance metric. Below, we show this point by proving distance conditions (ii).

Since  $\sum_{i=1}^n \Delta p_i^A$  equals zero owing to the normalization condition, the second-order approximation of the Taylor expansion of KL divergence becomes

$$D(O \parallel \alpha) \approx D(\alpha \parallel O) \approx \sum_{i=1}^n \frac{(\Delta p_i^\alpha)^2}{2p_i^O} > 0, \quad (8)$$

thereby satisfying condition (ii-a). Furthermore, we introduce point  $\beta$ , situated on the mixture geodesic [29] (m-geodesic) connecting points O and B (Fig. 1(b)). The m-geodesic is an affine line with respect to  $\boldsymbol{\eta}$ ; therefore,, point  $\beta$  and tangent vector  $\boldsymbol{\omega}$  along this line can be expressed as

$$\eta_i^\beta = \eta_i^O + t(\eta_i^B - \eta_i^O) \quad (0 \leq t \leq 1) \quad \text{and} \quad \boldsymbol{\omega} = \sum_{i=1}^{n-1} (\eta_j^B - \eta_j^O) \partial / \partial \eta_j, \quad (9)$$

respectively. When e- and m- geodesics are orthogonal at point O, the inner product of the tangent vectors  $\mathbf{v}$  and  $\boldsymbol{\omega}$ ,  $g_n(\mathbf{v}, \boldsymbol{\omega})$ , becomes 0. Therefore, by substituting Eqs. (3–9) into the aforementioned orthogonal relation, the Pythagorean theorem (ii-b) can be obtained [30,31]:

$$D(\alpha \parallel \beta) = D(O \parallel \alpha) + D(O \parallel \beta). \quad (10)$$

When the e- and m-geodesics are not orthogonal, the sum of the square roots of KL divergence becomes

$$\begin{aligned} \sqrt{D(O \parallel \alpha)} + \sqrt{D(O \parallel \beta)} &\approx \sqrt{\sum_{i=1}^n \frac{(\Delta p_i^\alpha)^2}{2p_i^O}} + \sqrt{\sum_{i=1}^n \frac{(\Delta p_i^\beta)^2}{2p_i^O}} \\ &\geq \sqrt{\sum_{i=1}^n \frac{(\Delta p_i^\alpha - \Delta p_i^\beta)^2}{2p_i^O}} \approx \sqrt{D(\alpha \parallel \beta)}, \end{aligned} \quad (11)$$

satisfying the triangle inequality (ii-c) as well. Eqs. (8), (10), and (11) demonstrate that any

infinitesimal change along the e-geodesic connecting two points satisfies Euclidean distance conditions (ii).

Next, we establish the reverse relationship: when the Euclidean space conditions are satisfied on the line connecting points O and A, the line becomes an e-geodesic. Consider a set of points, denoted as set  $\Omega$ , whose KL divergences from point A have the same value with  $D(O\|A)$ . Since the Euclidean nature is preserved between points O and A, with point O being a member of the set  $\Omega$ , both the set and point A hold Euclidean properties. In Euclidean space, a set of points equidistant from a center forms a hypersphere, with the normal vector on the surface pointing toward the center. Analogously, set  $\Omega$  also forms a hypersphere, with any normal vector on the surface pointing toward the center, point A. Then, the  $i^{\text{th}}$  component of the line connecting points O and A becomes

$$\left\{-\nabla_{\boldsymbol{\eta}} D(O\|A)\right\}_i = -\frac{\partial D(O\|A)}{\partial \eta_i} = \theta_i^A - \theta_i^O \quad (12)$$

A comparison of Eq. (12) and Eq. (7) reveals that the line is e-geodesic.

Finally, we formulate the gradient descent method in  $\mathbf{p}$ -space by assuming that the geometry of the gradient descent path in a general Euclidean space [30] holds between two points on the approximate Euclidean path. We utilize the  $\boldsymbol{\eta}$  coordinate system to describe the  $\mathbf{p}$ -space, with  $\boldsymbol{\eta}^k$  and  $\boldsymbol{\eta}^{k+1}$  representing the model probability distributions after the  $k^{\text{th}}$  and  $k+1^{\text{th}}$  transformations through the gradient descent, respectively (Fig. 1(c)). Furthermore, let  $\Gamma^k$  be the contour of  $\Phi(\boldsymbol{\eta})$  passing through  $\boldsymbol{\eta}^k$ , and let  $\Omega^{k+1}$  be the hypersphere centered at  $\boldsymbol{\eta}^{k+1}$  with radius  $a^{k+1}$ , a parameter to be determined. As demonstrated in the gradient descent path within the general Euclidean space [30], the relationship between two points on the path can be described by the geometric connection between the contour  $\Gamma^k$  and hypersphere  $\Omega^{k+1}$ , which are tangent at point  $\boldsymbol{\eta}^k$ . That is,  $\boldsymbol{\eta}^k$  represents the extremum on  $\Omega^{k+1}$  (Fig. 1(c) and Fig. S1 in [31]). Analogously, the gradient descent for the  $\mathbf{p}$ -space can be determined by identifying the extremum of the Lagrangian expressed as follows:

$$L(\boldsymbol{\eta}^k) = \Phi(\boldsymbol{\eta}^k) + (a^{k+1} - D(k+1\|k))/\tau \quad (13)$$

The extremum can be determined by solving  $\nabla_{\boldsymbol{\eta}^k} L(\boldsymbol{\eta}^k) = 0$  with Eq. (12), resulting

$$\Delta\theta = -\tau\nabla_{\eta}\Phi. \quad (14)$$

One advantage of Eq. (14) is its simplicity in determining the normalization constant. This can be demonstrated by rewriting Eq. (14) in the form of Eq. (2). From Eq. (4), each component of Eq. (14) becomes

$$\Delta\log p_i + \tau \frac{\partial\Phi}{\partial p_i} = \Delta\log p_n + \tau \frac{\partial\Phi}{\partial p_n}. \quad (15)$$

Eq. (15) is valid for all  $1 \leq i \leq n-1$ ; hence, the right-hand side can be regarded as a normalization constant  $C$ . Consequently, the normalization condition after the transformation provides the formulation for  $C$ , reducing Eq. (15) to Eq. (2).

### Setup for estimation simulations

To assess the validity of Eq. (2), we conducted simulations, in which protein conformational ensembles were reconstructed from pseudo-experimental SAXS data,  $I^{\text{EXP}}(Q)$  ( $Q = 4\pi \sin\theta/\lambda$ , where  $\lambda$  and  $2\theta$  represent the wavelength of the incident X-ray beam and scattering angle, respectively). The observables in this case can be represented as  $\mathbf{Y} = (I^{\text{EXP}}(Q_1), I^{\text{EXP}}(Q_2), \dots, I^{\text{EXP}}(Q_m))$ . SAXS data are sensitive to motions of an entire protein structure [31-33], making it useful for reconstructing ensembles related to such motions. For our study, we utilized transferrin as a model protein system [34,35], comprising two domains (Fig. 2(a)). Through all-atom molecular dynamics (MD) simulations, the primary motion of transferrin involves an open-close movement between the domains (Fig. S2 in [30]). Consequently, the ensemble can be simplified as a one-dimensional distribution based on the distance between domains,  $R_{\text{CM}}$  (Fig. 2(b)). In the reconstruction simulations, conformations within each bin of 0.2 Å on  $R_{\text{CM}}$  were grouped into a single conformational state, as substantial differences in SAXS data were observed among states of this size (Fig. S3 in [31]). Denoting the  $j^{\text{th}}$  SAXS data of the  $i^{\text{th}}$  state as  $I_i(Q_j)$ , the corresponding data for the model ensemble  $\mathbf{p}^{\text{A}}$  becomes  $I(Q_j \parallel \mathbf{p}^{\text{A}}) = \sum_{i=1}^n p_i^{\text{A}} I_i(Q_j)$ .



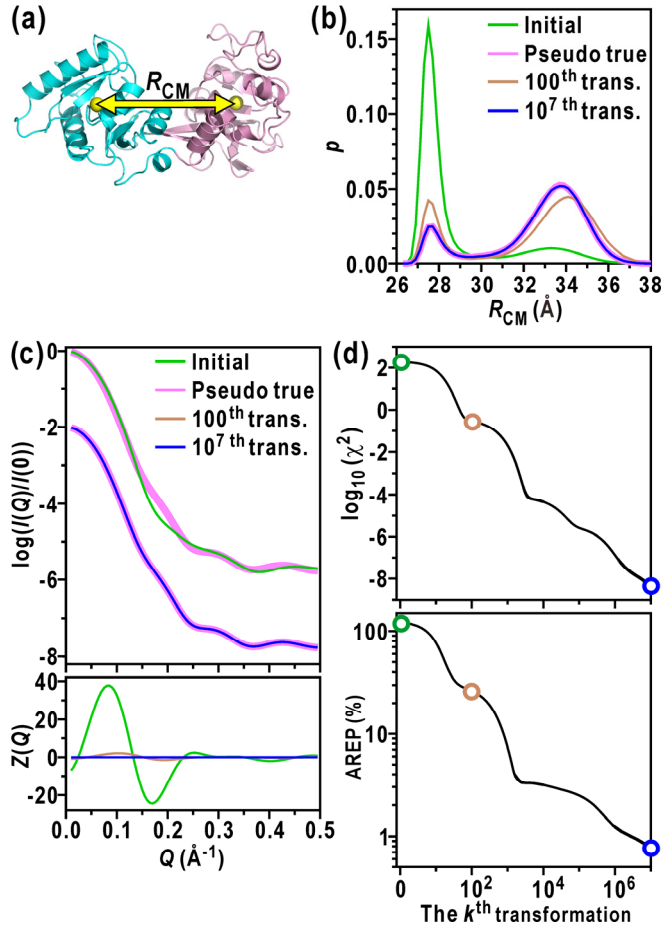


**FIG. 2.** Results of the numerical simulations with the small transformation rate  $\delta$  of 0.00025. (a) Transferrin as a model system for the reconstruction simulations. The domain distance  $R_{CM}$  represents the distance between the mass centers of the two domains. (b) Comparisons of the pseudo-true, initial and reconstructed probability distributions on  $R_{CM}$ . (c) Comparisons of the SAXS data (upper panel). The residuals between the pseudo-experimental and estimated data were evaluated using  $z(Q) = \{I(Q \| \mathbf{p}) - I^{\text{EXP}}(Q)\} / \sigma(Q)$  (lower). (d) Evolution of probability distribution through iterative transformations monitored using  $\chi^2$  (upper) and AREP (lower).

By employing the multiple-Gō coarse-grained molecular dynamics (CGMD) simulations [37], we generated two model ensembles, with the primary populations located at closed and open conformational states (Fig. 2(b)) (referred to as closed and open ensembles, respectively). The closed ensemble was utilized as the initially modeled ensemble  $\mathbf{p}^0$  for the reconstruction simulations, from which an ensemble was iteratively transformed using Eq. (2). The open ensemble served as a pseudo-

true ensemble  $\mathbf{p}^{\text{true}}$ , from which the pseudo-experimental SAXS data  $I^{\text{EXP}}(Q)$  [37] were generated (Fig. 2(c)). The simulation setup allowed for the quantitative assessment of the validity of Eq. (2) by investigating to what extent  $I^{\text{EXP}}(Q)$  and  $\mathbf{p}^{\text{true}}$  were reproduced.

The objective functional for SAXS data is denoted as  $\chi^2$  [39] expressed as follows:

$$\chi^2(\mathbf{p}) = \frac{1}{M} \sum_{j=1}^M \left[ \frac{I(Q_j | \mathbf{p}) - I^{\text{EXP}}(Q_j)}{\sigma(Q_j)} \right]^2, \quad (16)$$

where  $\sigma(Q)$  denote the  $Q$ -dependent experimental errors (Eq. (S8) in [31]). In the simulations, we chose not to introduce noise into  $I^{\text{EXP}}(Q)$  for simplicity. Therefore, the complete reproduction of SAXS data provides  $\chi^2$  value of 0. By substituting  $\chi^2$  into Eq. (2), we iteratively transform a model ensemble from the initial ensemble  $\mathbf{p}^0$ . The ensemble at the  $k^{\text{th}}$  transformation is designated as  $\mathbf{p}^k$ , hereinafter. The accuracy of  $\mathbf{p}^k$  was assessed using the averaged relative error of  $\mathbf{p}^k$  (AREP) expressed as  $\text{AREP} = \sum_{i=1}^N |p_i^k - p_i^{\text{true}}|$ . The complete reproduction of  $\mathbf{p}^{\text{true}}$  provides an AREP value of 0.

### Validation of Eq. (2) through reconstruction simulations

In the simulation with the small transformation rate  $\tau$  of 0.00025, the application of Eq. (2) successfully reproduced both the SAXS data  $I^{\text{EXP}}(Q)$  (Fig. 2(c)) and pseudo-true ensemble  $\mathbf{p}^{\text{true}}$  (Fig. 2(b)), demonstrating the theoretical validity of our approach. The evolution of the ensemble through iterative transformation was monitored using  $\chi^2$  and AREP (Fig. 2(d)). Up to the 100<sup>th</sup> transformation,  $\chi^2$  rapidly decreased to less than 0.3 (brown circle in Fig. 2(d)), indicating progress toward reproducing the pseudo-true ensemble. Subsequently, the evolution continued toward asymptotically achieving complete reproduction of both  $I^{\text{EXP}}(Q)$  and  $\mathbf{p}^{\text{true}}$  (blue circle in Fig. 2(d)).

To investigate the Euclidean space property, we compared  $D(k||k+1)$  and  $D(k+1||k)$ , which represent the KL divergence from  $\mathbf{p}^k$  and  $\mathbf{p}^{k+1}$  and its reverse, respectively. When the transformation rate  $\tau$  was small, the Euclidean property  $D(k||k+1) = D(k+1||k) > 0$  was consistently observed throughout all transformations (Fig. 3(a)), resulting in excellent convergence in optimization (Fig. 2). Conversely, when the step size was too large ( $\tau = 0.025$ ), the relationship of  $D(k||k+1) = D(k+1||k)$

did not hold (Fig. 3(b)), resulting in the failure of optimization to reproduce both  $I^{\text{EXP}}(Q)$  and  $\mathbf{p}^{\text{true}}$  (Fig. S4 in [31]).

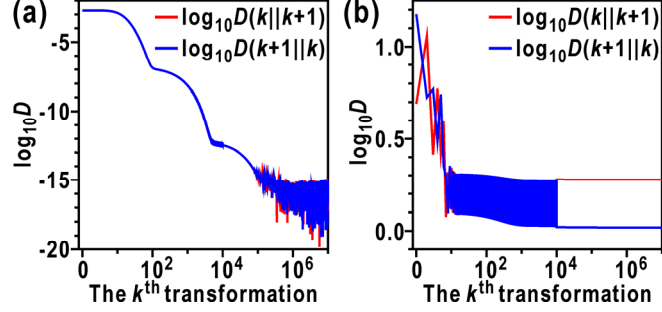


**FIG. 3.** Evolutions of  $D(k||k+1)$  and  $D(k+1||k)$  in the simulations using the  $\delta$  values of (a) 0.00025 and (b) 0.025.

In contrast to calculations using Eq. (2), the gradient descent formulations based on Eq. (1) failed to reproduce both the pseudo-true ensemble and SAXS data, regardless of the value of  $\tau$ . The two formulations used were expressed as follows:

$$\Delta \mathbf{p} \propto -\tau \nabla_{\mathbf{p}} \Phi(\mathbf{p}), \quad (17)$$

and

$$\Delta \log \mathbf{p} \propto -\tau \nabla_{\log \mathbf{p}} \Phi(\mathbf{p}). \quad (18)$$

When utilizing Eq. (17), the optimization diverged immediately after the initial transformation. The optimization using Eq. (18) resulted in a decrease in both  $\chi^2$  and AREP at the initial transformations but diverged after reaching an  $\chi^2$  value of 1.1, failing to reproduce  $\mathbf{p}^{\text{true}}$  (Fig. S5 in [31]). To prevent such divergence, constraints on the initial ensemble  $\mathbf{p}^0$  were introduced into the objective functional  $\Phi$ . These constraints were implemented by adding a relative entropy term from the initial model as follows:

$$\Phi(\mathbf{p}) = \chi^2(\mathbf{p}) + \kappa \sum_{i=1}^n p_i \log \frac{p_i}{p_i^0}, \quad (19)$$

where  $\kappa$  denotes the confidence factor for the initial model ensemble [15-17]. The implementation of constraints prevented divergence (Fig. S6 in [31]), and a moderate value of  $\kappa$  resulted in improvements in the reproduction of  $\mathbf{p}^{\text{true}}$  and  $I^{\text{EXP}}(Q)$  (Fig. 4). However, even the optimal value of  $\kappa$

could not achieve complete reproduction. Furthermore, the introduction of constraints in the calculations using Eq. (2) further degraded the accuracy of the reproduction, indicating their inclusion unnecessary.

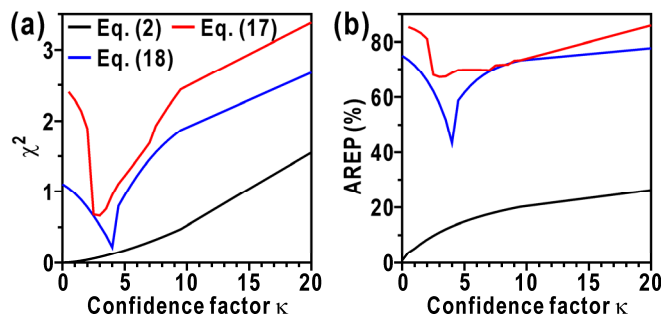


**FIG. 4.** Dependence of simulation results on confidence parameter  $\kappa$ . (a)  $\chi^2$  and (b) AREP are monitored. The red, blue, and black curves represent the results using Eqs. (2), (17) and (18), respectively.

Consequently, the present numerical simulations demonstrated that only Eq. (2) exhibited excellent convergence in optimizing probability distribution, even when utilizing noiseless experimental data. Furthermore, constraints on an initially modeled probability distribution  $\mathbf{p}^0$  to prevent divergence were fundamentally unnecessary for accurately reconstructing the true distribution.

## Discussion

In this study, we developed a gradient descent in the p-space by considering its manifold nature. Numerical simulations reconstructing protein conformational ensembles from SAXS data demonstrated the excellent convergence behavior of the formulation in optimization, thereby successfully reproducing the true probability distribution. Poor convergence with high transformation rates  $\tau$ , or when employing Euclidean gradient descent (Eqs (17) and (18)), indicate that transforming a probability distribution under a gradient field should be an infinitesimal displacement along an e-geodesic. Notably, a major limitation of our simulations is that the influence of noise was not considered in the pseudo-experimental data. To fully validate the applicability of our findings, we are

currently conducting studies using noisy experimental data. The results will be presented in a different report.

Regarding the utility of the optimization, another point to be addressed is the case of the initially modeled distribution  $\mathbf{p}^0$  deviating significantly from the true probability distribution  $\mathbf{p}^{\text{true}}$  in the  $\mathbf{p}$ -space. In this case, two approaches will be necessary. First, experimental data to be implemented into an objective functional should be increased. Concerning protein conformational ensembles, various experimental techniques such as solution neutron scattering [40], nuclear magnetic resonance [41-44], and cryo-electron microscopy [45,46] are available. Integrating these diverse data sources can be highly beneficial [47-49]. The second approach involves comprehensively sampling the  $\mathbf{p}$ -space under an objective functional. Our research highlighted the necessity of considering the manifold structure of the  $\mathbf{p}$ -space in sampling. Therefore new techniques such as Monte-Carlo moving on the manifold should be developed in future studies.

Reconstructing probability distributions from observed data is crucial in scientific research and machine learning [10,11]. The excellent convergence behavior of Eq. (2) holds significant practical value across various fields. Furthermore, the transformation of probability distributions is a topic of interest in non-equilibrium physics [50,51] and mathematical statistics [21,52]. Our findings on the transformation of probability distribution under a gradient field can provide valuable insights for these areas of study.

## **Acknowledgements**

This study was supported by grants from the Japan Society for the Promotion of Science (26104535, 26800227, 17K19209, 17H04854, and 21K03489 to T. O.; 18H05229 to T. O., R. I., and M. S.).

## References

1. S. J. L. Billinge and K. M. Ø. Jensen, *Atomic pair distribution function analysis: a primer*, Vol. 22 (Oxford University Press, Oxford, 2023).
2. K. Amini, A. Rouzée and M. J. J. Vrakking, *Structural dynamics with X-ray and electron scattering* (The Royal Society of Chemistry, London, 2024).
3. S. Tokuda, S. Souma, K. Sagawa, T. Takahashi, Y. Ando, T. Nakanishi and T. Sato, Unveiling quasiparticle dynamics of topological insulators through Bayesian modeling, *Comm. Phys.* **4**, 170 (2021).
4. R. Sweke, J.-P. Seifert, D. Hangleiter and J. Eisert, On the quantum versus classical learnability of discrete distributions, *Quantum* **5**, 417 (2021).
5. M. Bonomi, G. T. Heller, C. Camilloni, M. Vendruscolo, Principles of protein structural ensemble determination, *Curr. Opin. Struct. Biol.* **42**, 106-116 (2017).
6. T. Isaac, N. Petra, G. Stadler and O. Ghattas, Scalable and efficient algorithms for the propagation of uncertainty from data through inference to prediction for large-scale problems, with application to flow of the Antarctic ice sheet, *J. Comput. Phys.* **296**, 348 (2015).
7. T. Schneider, S. Lan, A. Stuart and J. Teixeira, Earth system modeling 2.0: a blueprint for models that learn from observations and targeted high-resolution simulations, *Geophys. Res. Lett.* **44**, 396 (2017).
8. K. Yuen, *Bayesian methods for structural dynamics and civil engineering* (John Wiley & Sons, Singapore, 2010).
9. S. Cao and D. Z. Huang, Bayesian calibration for large-scale fluid structure interaction problems under embedded/immersed boundary framework, *Int. J. Numer. Methods Eng.* **123**, 1791 (2022).
10. C. M. Bishop, *Pattern recognition and machine learning* (Springer, New York, 2006).
11. K. P. Murphy, *Machine learning: a probabilistic perspective* (The MIT Press, Cambridge, 2012).
12. A. Gelman, J. B. Carlin, H. S. Stern, D. B. Dunson, A. Vehtari and D. B. Rubin, *Bayesian data analysis*, (Chapman and Hall/CRC, Boca Raton, 2013).
13. M. Hollander, D. A. Wolfe and E. Chicken, *Nonparametric statistical methods* (John Wiley &

Sons, Inc., New Jersey, 2014).

14. H. B. Curry, The method of steepest descent for non-linear minimization problems, *Quart. Appl. Math.* **2**, 258 (1944).
15. A. Cesari, S. Reißer and G. Bussi, Using the maximum entropy principle to combine simulations and solution experiments, *Computation* **6**, 15 (2018).
16. S. Bottaro, T. Bengsten and K. Lindorff-Larsen, Integrating molecular simulation and experimental data: A Bayesian/maximum entropy reweighting approach, *Methods Mol. Biol.* **2112**, 219 (2020).
17. J. Köfinger, L. S. Stelzl, K. Reuter, C. Allande, K. Reichel and G. Hummer, Efficient ensemble refinement by reweighting, *J. Chem. Theory Comput.* **15**, 3390 (2019).
18. S. Amari and H. Nagaoka, *Methods of information geometry*, Vol. 191 (Oxford University, New York, 2000).
19. S. Amari, Natural gradient works efficiently in learning, *Neural Compute.* **10**, 251 (1998).
20. G. Hummer and J. Köfinger, Bayesian ensemble refinement by replica simulations and reweighting, *J. Chem. Phys.* **143**, 243150 (2015).
21. Y. Chen, D. Z. Huang, J. Huang, S. Reich and A. M. Stuart, Sampling via gradient flows in the space of probability measures, arXiv :2310.03597v3.
22. S. Kobayashi and K. Nomizu, *Foundations of differential geometry, I, II*, (Interscience, New York, 1963, 1969).
23. H. Nagaoka and S. Amari, Differential geometry of smooth families of probability distributions, Technical Report METR 82-7 (Dept. of Math. Eng. And Inst. Phys., Univ. of Tokyo, 1982).
24. S. Amari, *Differential-geometric methods in statistics*, vol. 28 (Springer, Berlin, 1985).
25. R. A. Fisher, Theory of statistical estimation, *Math. Proc. Camb. Philos. Soc.* **22**, 700 (1925).
26. C. R. Rao, Information and accuracy attainable in the estimation of statistical parameters, *Bull. Calcutta. Math. Soc.* **37**, 81 (1945).
27. S. Kullback and R. A. Leibler, On information and sufficiency. *Ann. Math. Stat.* **22**, 79 (1951).
28. S. Eguchi, Second order efficiency of minimum contrast estimators in a curved exponential family,

- Ann. Stat. **11**, 793 (1983).
29. S. Eguchi, A characterization of second order efficiency in a curved exponential family, Ann. Inst. Stat. Math. **36**, 199 (1984).
  30. S. Amari, Differential geometry of curved exponential families—curvature and information loss, Ann. Stat. **10**, 357 (1982).
  31. See Supplementary Material for proof of the Pythagorean theorem for points on  $e$ - and  $m$ -geodesics, geometries of gradient descent path in a general Euclidean space, all-atom MD simulation of transferrin, Coarse-grained MD simulations of transferrin, analyses on conformational motions of transferrin, calculation of SAXS data from CGMD simulations,  $Q$ -dependent experimental errors of SAXS data, dependencies of the calculated SAXS data of transferrin on conformational changes, and results of reconstruction simulations beyond those shown in Fig. 2 (Figs. S4-S6).
  32. C. D. Putnam, M. Hammel, G. L. Hura and J. A. Tainer, X-ray solution scattering (SAXS) combined with crystallography and computation: defining accurate macromolecular structures, conformations and assemblies in solution, Q. Rev. Biophys. **40**, 191 (2007).
  33. M. Hammel, Validation of macromolecular flexibility in solution by small-angle X-ray scattering (SAXS), Eur. Biophys. J. **41**, 789 (2012).
  34. T. Oroguchi, H. Hashimoto, T. Shimizu, M. Sato, and M. Ikeguchi, Intrinsic dynamics of restriction endonuclease EcoO109I studied by molecular dynamics simulations and X-ray scattering data analysis, Biophys. J. **96**, 2808 (2009).
  35. R. T. A. MacGillivray, S. A. Moore, J. Chen, B. F. Anderson, H. Baker, Y. Luo, M. Bewley, C. A. Smith, M. E. P. Murphy, Y. Wang, A. B. Mason, R. C. Woodworth, G. D. Brayer and E. N. Baker, Two high-resolution crystal structures of the recombinant N-lobe of human transferrin reveal a structural change implicated in iron release, Biochemistry **37**, 7919-7928 (1998).
  36. P. D. Jeffrey, M. C. Bewley, R. T. A. MacGillivray, A. B. Mason, R. C. Woodworth and E. N. Baker, Ligand-induced conformational change in transferrins: crystal structure of open form of the N-terminal half-molecule of human Transferrin, Biochemistry **37**, 13978 (1998).



37. H. Kenzaki, N. Koga, N. Hori, R. Kanada, W. Li, K. Okazaki, X. Q. Yao and S. Takada, CafeMol: a coarse-grained biomolecular simulator for simulating proteins at work, *J. Chem. Theory Comput.* **7**, 1979 (2011).
38. T. Ekimoto, Y. Kokabu, T. Oroguchi and M. Ikeguchi, Combination of coarse-grained molecular dynamics simulations and small-angle X-ray scattering experiments, *Biophys. Physicobiol.* **16**, 377 (2019).
39. D. I. Svergun, C. Barberato and M. H. J. Koch, CRY SOL – a program to evaluate X-ray solution scattering of biological macromolecules from atomic coordinates, *J. Appl. Cryst.* **28**, 768 (1995).
40. M. Sonntag, P. K. A. Jagtap, B. Simon, M. Appavou, A. Geerlof, R. Stehle, F. Gabel, J. Hennig and M. Sattler, Segmental, domain-selective perdeuteration and small-angle neutron scattering for structural analysis of multi-domain proteins, *Angew. Chem. Int. Ed.* **56**, 9322 (2017).
41. E. Z. Eisenmesser, O. Millet, W. Labeikovsky, D. M. Korzhnev, M. Wolf-Watz, D. A. Bosco, J. J. Skalicky, L. E. Kay and D. Kern, Intrinsic dynamics of an enzyme underlies catalysis, *Nature* **438**, 117 (2005).
42. T. R. Alderson and L. E. Kay, NMR spectroscopy captures the essential role of dynamics in regulating biomolecular function. *Cell* **184**, 577 (2021).
43. A. G. Palmer III, Enzyme dynamics from NMR spectroscopy, *Acc. Chem. Res.* **48**, 457 (2015).
44. L. Yu and R. Brüschweiler, Quantitative prediction of ensemble dynamics, shapes and contact propensities of intrinsically disordered proteins, *PLOS Comput. Biol.* (2022).
45. A. Dashti, G. Mashayekhi, M. Shekhar, D. B. Hail, S. Salah, P. Schwander, A. des Georges, A. Singharoy, J. Frank and A. Oumazd, Retrieving functional pathways of biomolecules from single-particle snapshots, *Nat. Comm.* **11**, 4734 (2020).
46. M. Oide, T. Kato, T. Oroguchi and M. Nakasako, Energy landscape of domain motion in glutamate dehydrogenase deduced from cryo-electron microscopy, *FEBS J.* **287**, 3472 (2020).
47. N. Sibille and P. Bernadó, Structural characterization of intrinsically disordered proteins by the combined use of NMR and SAXS, *Biochem. Soc. Trans.* **40**, 955 (2012).
48. A. G. Kikhney and D. I. Svergun, A practical guide to small angle X-ray scattering (SAXS) of

flexible and intrinsically disordered proteins, FEBS Lett. **589**, 2570 (2015).

49. M. Chan-Yao-Chong, D. Durand and T. Ha-Duong, Molecular dynamics simulations combined with nuclear magnetic resonance and/or small-angle X-ray scattering data for characterizing intrinsically disordered protein conformational ensembles, J. Chem. Inf. Model **59**, 1743 (2019).
50. M. Nakazato and S. Ito, Geometrical aspects of entropy production in stochastic thermodynamics based on Wasserstein distance, Phys. Rev. Research **3**, 043093 (2021).
51. T. V. Vu and K. Saito, Thermodynamic unification of optimal transport: thermodynamic uncertainty relation, minimum dissipation, and thermodynamic speed limits, Phys. Rev. X **13**, 011013 (2023).
52. Y. Wang and W. Li, Accelerated information gradient flow, J. Sci. Comput. **90**, 1 (2022).

## Supplementary Material: Manifold-based transformation of the probability distribution for convergence in optimization

Tomotaka Oroguchi<sup>a,b\*</sup>, Rintaro Inoue<sup>c</sup>, and Masaaki Sugiyama<sup>c</sup>

<sup>a</sup>Department of Physics, Faculty of Science and Technology, Keio University, 3-14-1 Hiyoshi, Kohoku-ku, Yokohama 223-8522, Japan.

<sup>b</sup>RIKEN SPring-8 Center, 1-1-1 Kouto, Sayo-cho, Sayo-gun, Hyogo 679-5148, Japan

<sup>c</sup>Institute for Integrated Radiation and Nuclear Science, Kyoto University, Kumatori, Sennan-gun, Osaka 590-0494 Japan.

\*Corresponding author

oroguchi@phys.keio.ac.jp

### Proof of Pythagorean theorem for points on e- and m-geodesics

This section proves that the points on e- and m-geodesics satisfies the Pythagorean theorem, as shown in Eq. (10), when these geodesics are orthogonal. The proof utilizes points, O,  $\alpha$ , and  $\beta$ , as referred to in the main text. By substituting Eqs. (5), (7), and (9) into the Fisher information metric, Eq. (3), we obtain

$$\sum_{i=1}^{n-1} (\theta_i^\alpha - \theta_i^O) (\eta_i^\beta - \eta_i^O) = 0. \quad (\text{S1})$$

By substituting Eq. (4), the left-hand side of Eq. (S1) can be expressed using the KL divergence as follows:

$$\begin{aligned} \sum_{i=1}^{n-1} (\theta_i^\alpha - \theta_i^O) (\eta_i^\beta - \eta_i^O) &= \left( \sum_{i=1}^{n-1} \theta_i^\alpha \eta_i^\beta + \log p_n^\alpha \right) - \left( \sum_{i=1}^{n-1} \theta_i^\alpha \eta_i^O + \log p_n^\alpha \right) \\ &\quad - \left( \sum_{i=1}^{n-1} \theta_i^O \eta_i^\beta + \log p_n^O \right) + \left( \sum_{i=1}^{n-1} \theta_i^O \eta_i^O + \log p_n^O \right) \\ &= \left\{ \sum_{i=1}^{n-1} p_i^\beta \log p_i^\alpha + \left( 1 - \sum_{i=1}^{n-1} p_i^\beta \right) \log p_n^\alpha \right\} - \left\{ \sum_{i=1}^{n-1} p_i^O \log p_i^\alpha + \left( 1 - \sum_{i=1}^{n-1} p_i^O \right) \log p_n^\alpha \right\} \\ &\quad - \left\{ \sum_{i=1}^{n-1} p_i^\beta \log p_i^O + \left( 1 - \sum_{i=1}^{n-1} p_i^\beta \right) \log p_n^O \right\} + \left\{ \sum_{i=1}^{n-1} p_i^O \log p_i^O + \left( 1 - \sum_{i=1}^{n-1} p_i^O \right) \log p_n^O \right\}. \\ &= \sum_{i=1}^n p_i^\beta \log p_i^\alpha - \sum_{i=1}^n p_i^O \log p_i^\alpha - \sum_{i=1}^n p_i^\beta \log p_i^O + \sum_{i=1}^n p_i^O \log p_i^O \\ &= -\sum_{i=1}^n p_i^\beta \log \frac{p_i^\beta}{p_i^\alpha} + \sum_{i=1}^n p_i^O \log \frac{p_i^O}{p_i^\alpha} + \sum_{i=1}^n p_i^\beta \log \frac{p_i^\beta}{p_i^O} \\ &= -D(\beta \| \alpha) + D(O \| \alpha) + D(\beta \| O) \end{aligned}$$

(S2)

Therefore, by substituting Eq. (S2) and Eq. (8) into Eq. (S1), we can derive the Pythagorean theorem, Eq. (10).

### Geometrics of gradient descent path in general Euclidean space

This section delves into the geometric properties of the gradient descent path in general Euclidean space  $\xi$ . To achieve this, we examine the geometric relation between two points  $\xi^k$  and  $\xi^{k+1}$  on the path, representing the positions after the  $k^{\text{th}}$  and  $k+1^{\text{th}}$  transformations through gradient descent, respectively (Fig. S1). The gradient descent formulation in Eq. (1) can be expressed using the Euclidean distance between these points,  $d(k||k+1)$ , as

$$\nabla_{\xi^k} \left( \Phi(\xi^k) - d(k+1||k)/\tau \right) = 0. \quad (\text{S3})$$

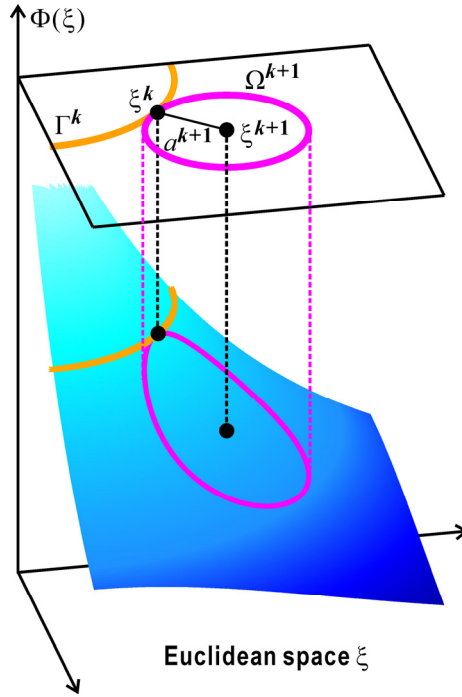


**FIG. S1.** Geometry of gradient descent path in general Euclidean space  $\xi$ .

Mathematically, Eq. (S3) is equivalent to determining the extremum of a Lagrangian of the form:

$$L = \Phi(\xi^k) + (a^{k+1} - d(k+1||k))/\tau, \quad (\text{S4})$$

where  $a^{k+1}$  denotes a parameter to be determined. In the general Lagrange multipliers method,  $\xi^{k+1}$  and  $a^{k+1}$  are known, whereas  $\xi^k$  and  $1/\tau$  denote the position and multiplier to be determined, respectively. In this scenario, determining the extremum of the Lagrangian, Eq. (S4), is equivalent to determining the extremum of  $\Phi(\xi)$  on the hypersphere  $\Omega^{k+1}$  defined by the constraint  $a^{k+1} - d(k+1||k) = 0$  (Fig.

S1). However, in gradient descent, the relationship between the variables is reversed:  $\xi^k$  and  $1/\tau$  are known, whereas  $\xi^{k+1}$  and  $a^{k+1}$  represent the position and parameter to be determined, respectively. Therefore, when  $\Gamma^k$  is defined as the contour of  $\mathcal{D}(\xi)$  passing through  $\xi^k$ , determining the extremum of Lagrangian, Eq. (S4), becomes equivalent to determining the hypersphere  $\Omega^{k+1}$  tangential to  $\Gamma^k$  at the point  $\xi^k$  (Fig. S1). This represents the geometric relationship that must be satisfied between the two points  $\xi^k$  and  $\xi^{k+1}$  along the gradient descent path. We assume that this geometric relationship also applies to the two points  $\eta^k$  and  $\eta^{k+1}$  on the gradient path in the  $\mathbf{p}$ -space, particularly when these points are in an approximately Euclidean relationship. This assumption is expressed using Eq. (13) in the main text.

### All-atom MD simulation of transferrin

The all-atom MD (AAMD) simulation was conducted using the AMBER16 [1] software package with the AMBER ff15FB [2] force field and TIP3PFB [3] water model. The crystal structure of the apo form [4] (PDB ID: 1BP5) was utilized as the initial structure. The solution was prepared by placing the crystal structure in a truncated octahedron box and adding a 30 Å layer of water molecules. Na<sup>+</sup> and Cl<sup>-</sup> ions were introduced to neutralize the net charge of the system. Electrostatic interactions were handled using the particle-mesh Ewald method [5] with a real-space cutoff of 10 Å. Lennard–Jones interactions were truncated beyond 10 Å using a continuum model correction. Bonds involving hydrogen atoms were constrained using the SHAKE method [6], and a time step of 2 fs was set. Initially, the system was subjected to energy minimization of 1,000 steps. Subsequently, the temperature of the system was gradually increased from 10 K to 293 K in an NPT run of 300 ps at 1 atm. Finally, a 1- $\mu$ s NVT run was conducted for each production run. Simulations were conducted using NVIDIA TITAN V GPUs.

### Coarse-grained MD simulations of transferrin

For CGMD simulations, we used the off-lattice G $\ddot{o}$  model employed in the CafeMol software [7]. In this model, each amino acid residue was represented as a single CG particle located at the position of the C $_{\alpha}$  atom of the residue. The potential function is expressed as follows:

$$\begin{aligned}
V_{\text{G}\ddot{o}}(\mathbf{x}|\mathbf{x}_0) = & \sum_{i=1}^{n-1} K_{\text{bond}} (b_{i,i+1} - b_{i,i+1,0}) + \sum_{i=1}^{n-2} K_{\text{angle}} (\theta_{i,i+1,i+2} - \theta_{i,i+1,i+2,0}) \\
& + \sum_{i=1}^{n-3} \left\{ K_{\text{dihedral}}^{(1)} \left\{ 1 - \cos(\phi_{i,i+1,i+2,i+3} - \phi_{i,i+1,i+2,i+3,0}) \right\} \right. \\
& \left. + K_{\text{dihedral}}^{(3)} \left\{ 1 - \cos 3(\phi_{i,i+1,i+2,i+3} - \phi_{i,i+1,i+2,i+3,0}) \right\} \right\} \\
& + \sum_{i < j-3}^{\text{native contact}} \mathcal{E}_{\text{G}\ddot{o}} \left\{ 5 \left( \frac{r_{ij,0}}{r_{ij}} \right)^{12} - 6 \left( \frac{r_{ij,0}}{r_{ij}} \right)^{10} \right\} \\
& + \sum_{i < j-3}^{\text{non-native}} \mathcal{E}_{\text{ev}} \left( \frac{r_{ij,\text{repulsive}}}{r_{ij}} \right)^{12}
\end{aligned} \tag{S5}$$

where  $\mathbf{x}_0$  represents the 3D coordinates of the input structure. The bonded parameters are as follows:  $b_{i,i+1}$  and  $b_{i,i+1,0}$  represent the bond length between two neighboring residues and the corresponding length in  $\mathbf{x}_0$ , respectively;  $\theta_{i,i+1,i+2}$  and  $\theta_{i,i+1,i+2,0}$  denote the angle between three consecutive residues and the corresponding angle in  $\mathbf{x}_0$ , respectively;  $\phi_{i,i+1,i+2,i+3}$  and  $\phi_{i,i+1,i+2,i+3,0}$  denote the dihedral angle between four consecutive residues and corresponding dihedral angle in  $\mathbf{x}_0$ , respectively, with spring constants set to the values utilized in CafeMol [7]. The fourth term denotes the G $\bar{o}$  potential that maintains the conformational topology of  $\mathbf{x}_0$ . The G $\bar{o}$  term was calculated for any residue pair within a distance of  $r_{\text{native}}$  in  $\mathbf{x}_0$  (native contact pair).  $r_{ij}$  denotes the distance between native contact pairs  $i$  and  $j$ , whereas  $r_{ij,0}$  denotes the distance in  $\mathbf{x}_0$ . The cutoff distance  $r_{\text{native}}$  and force constant  $\varepsilon_{G\bar{o}}$  were adjusted to maintain the rigidity of a domain structure (root mean squared deviations of CG particles  $\leq 1.5$  Å) while enabling structural flexibility, such as domain motions during simulations. The fifth term represents the repulsive potential between residue pairs  $i$  and  $j$ , calculated for non-native contact pairs. The reference distance  $r_{ij,\text{repulsive}}$  depended on the amino acid residue types of  $i$  and  $j$ , and the cutoff distance  $r_{\text{repulsive}}$  was set to 2.0. The force constant  $\varepsilon_{\text{ev}}$  was set to 0.5 kcal/mol/Å<sup>12</sup>.

To generate a conformational ensemble that spanned apo and holo forms in each protein system, we utilized a multiple-G $\bar{o}$  CGMD simulation, with the potential expressed as follows:

$$V_{\text{multi-G}\bar{o}} \langle \mathbf{x} | \mathbf{x}_1, \mathbf{x}_2, \dots, \mathbf{x}_L \rangle = -k_B T \cdot \log \left\{ \sum_{i=1}^L \exp \left( -\frac{V_{G\bar{o}} \langle \mathbf{x} | \mathbf{x}_i \rangle + v_i}{k_B T_i} \right) \right\}, \quad (\text{S6})$$

where  $L$  is the number of input conformations and  $\mathbf{x}_i$  is the input coordinate of the  $i^{\text{th}}$  conformation.  $k_B$  and  $T$  are the Boltzmann constant and the simulation system temperature, respectively.  $T$  was set to 293 K in all multiple-G $\bar{o}$  CGMD simulations in this study. Parameter  $v_i$  determines the relative stability of the  $i^{\text{th}}$  conformation against the other conformations. The height of the free-energy barrier between the  $i^{\text{th}}$  and  $j^{\text{th}}$  conformations is determined by parameters  $T_i$  and  $T_j$ .

For reconstruction simulations, closed and open ensembles of transferrin were created using multiple-G $\bar{o}$  CGMD simulations. The crystal structures of the holo [8] (PDB ID: 1A8E) and apo [4] (PDB ID: 1BP5) forms were utilized as inputs to represent stable open and closed conformational states, respectively.

### Analyses on conformational motions of transferrin

Upon binding of an iron ion, transferrin undergoes the domain motion from an open to a closed conformations [4,8], suggesting that this motion of transferrin also occurred in the solution. To characterize the conformational motions of transferrin in the AAMD and CGMD simulation, we performed principal component analysis [9] (PCA) on the trajectories of these simulations. In these PCAs, the motions of the C-domain against the N-domain were evaluated using the  $C_\alpha$  best fits for the N-domain.

The first and second PC modes accounted for approximately 80% of the total  $C_\alpha$  mean square fluctuations in both the AAMD and CGMD simulations (Fig. S2(b)). These modes represented open-

close and twisting motions of the C-domain against the N-domain, respectively (Fig. S2(a)). Furthermore, strong correlations were observed for the first four PC modes between the AAMD and CGMD simulations (correlation coefficient  $> 0.9$ ), and certain correlations persisted up to the 8<sup>th</sup> PC mode (Fig. S2(c)). These results indicate that the domain motions between the AAMD and CGMD simulations were consistent, validating the effectiveness of the CGMD simulation in capturing large amplitude motions.

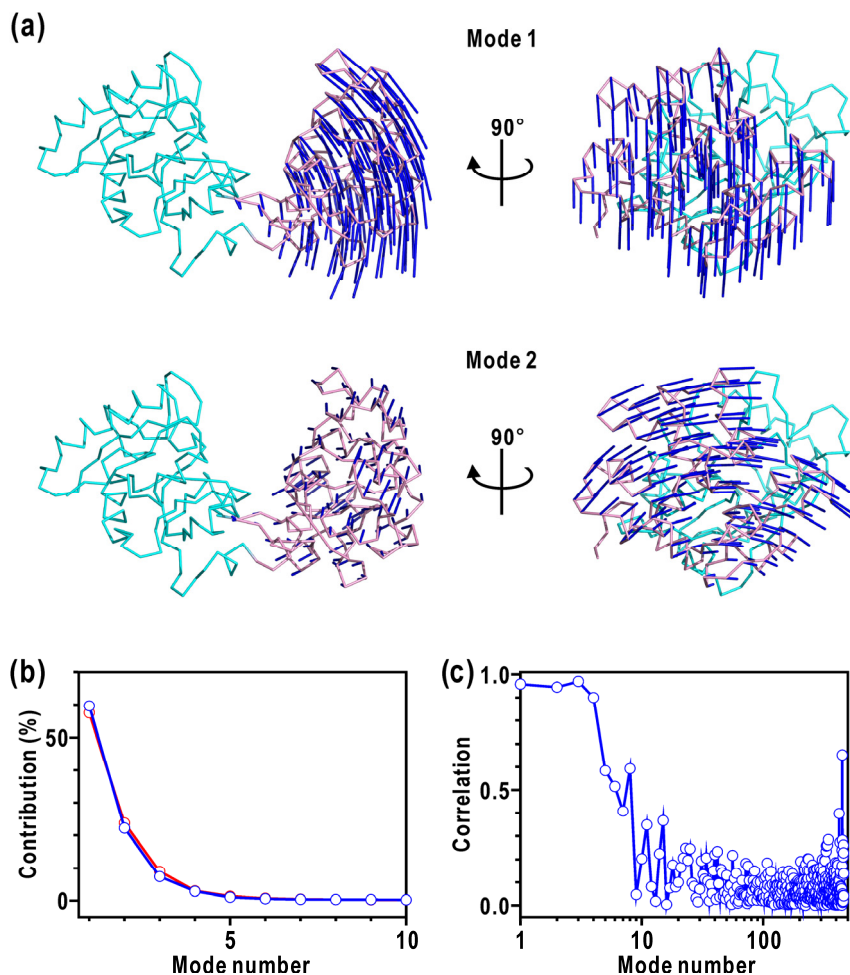


**FIG. S2.** Comparison of PCA in the AAMD and CGMD simulations of transferrin. (a) PCA modes calculated from AAMD trajectories: first PC mode (upper) and second PC mode (lower). The amplitude ( $3\sigma$ ) and direction of  $C_\alpha$  displacements along the first PC mode are represented by blue arrows. The domain structures are represented using different colors. (b) Individual contributions of the first 10 PC modes to total  $C^\alpha$ -mean square fluctuation in the AAMD (red) and CGMD (blue) simulations. (c) Correlation of the individual PC modes between AAMD and CGMD simulations.

### Calculation of SAXS data from CGMD simulations

We utilized the CGMD-SAXS method, as outlined in our previous study [10], to calculate the SAXS data from individual CG structures within the CGMD simulations. This method considered X-

ray scattering from both the solvent excluded by a protein molecule (solvent-excluded volume) and hydration shell, which is crucial for accurately calculating X-ray scattering from protein solutions. The previous study [10] demonstrated that the CGMD-SAXS data were consistent with not only experimental data but also the SAXS data calculated from AAMD trajectories.

To accurately calculate X-ray scattering from the solvent-excluded volume, the solvent parameter required is the electron density of the solvent in the bulk region ( $\rho$ ). For the hydration shell, the necessary parameters are the thickness and solvent density (hydration density) of the hydration layer. In the CGMD-SAXS method, the space surrounding a protein CG structure was divided into voxels with a side length  $\Delta D$  of 3 Å. Subsequently, voxels within the hydration layer were selected based on their distance from the CG structure. The scattering factor from each voxel of the hydration layer is expressed as follows:

$$f_{\text{hydration}}^{\text{CG}}(Q) = w\Delta D^3 f_{\text{water}}^{\text{CG}}(Q) \quad (\text{S7})$$

where  $w$  represents the increase in the number density of water molecules in the hydration layer from the bulk density.  $f_{\text{water}}^{\text{CG}}(Q)$  denotes the scattering factor of a single water molecule in an all-atom representation (one oxygen and two hydrogen atoms) and is expressed as follows:

$$f_{\text{water}}^{\text{CG}}(Q) = \left[ \sum_{i,j=1}^3 f_i(Q) f_j(Q) \frac{\sin(Qr_{ij})}{Qr_{ij}} \right]^{1/2} \quad (\text{S8})$$

To calculate Eq. (S8), we utilized the coordinates of the TIP3P water model were used. In the present reconstruction simulations, the solvent density parameters  $\rho$  and  $w$  were set to  $0.338 \text{ e}/\text{\AA}^3$  and  $0.112 \times 10^{-2} \text{ molecules}/\text{\AA}^3$ , respectively. Those values provide the good agreement with experimental SAXS data for model proteins [10]. All CGMD-SAXS calculations were conducted using NVIDIA TITAN V GPUs.

### **$Q$ -dependent experimental errors of SAXS data**

To investigate the  $Q$ -dependence of experimental errors, which is necessary for the calculation of  $\chi^2$  (Eq. (16)), we initially analyzed experimental SAXS data stored in the small angle scattering biological data bank [11]. All analyzed data were collected using modern single-photon counting detectors and varied in mass units and protein concentrations. Across all experimental data analyzed, the  $Q$ -dependence of the experimental errors  $\sigma^{\text{EXP}}(Q)$  can be approximated using the following model function:

$$\sigma^{\text{model}}(Q) = a I_{\text{Guinier}}^{\text{EXP}}(0) \left\{ I(Q) / I_{\text{Guinier}}^{\text{EXP}}(0) \right\}^b, \quad (\text{S9})$$

where  $I_{\text{Guinier}}^{\text{EXP}}(0)$  denotes the forward-scattering intensity estimated from the Guinier plot [12]. From Eq. (S9), the  $Q$ -dependent experimental errors in Eq. (16) in the main text can be modeled as



$$\sigma^{\text{EXP}}(Q) = aI^{\text{scaled}}(0) \left\{ I^{\text{scaled}}(Q) / I^{\text{scaled}}(0) \right\}^b, \quad (\text{S10})$$

with  $a = 0.003$  and  $b = 0.3$ , which are typical values observed in the analyzed experimental data.

### Dependencies of the calculated SAXS data of transferrin on conformational changes

To identify suitable coordinates for reconstructing transferrin conformational motions from SAXS data, we explored the correlation between the calculated SAXS data and conformational changes of this protein. The PC modes obtained through the PCA performed on the CGMD simulation (Fig. S3) were utilized to examine the conformational changes. Among these PC modes, the calculated SAXS data demonstrated dependencies only for the first two PC modes, which corresponded to domain motions. Therefore, we analyzed the dependence of the data on the 2D plane formed by these modes (Fig. S3(a)). All conformations within a 5 Å grid on this plane were categorized as a single conformational state represented by this grid. The SAXS data for each conformational state were calculated as the average of the data for all conformations within that state. This calculation utilized all conformations in broad ensembles 1 and 2 generated by the multiple-Gō CGMD simulations.

To assess the dependencies of the SAXS data, we conducted an analysis by calculating the  $\chi^2$  values for all pairs of conformational states. This process involved selecting a single conformational state on a plane, generating pseudo-experimental data from that state with Gaussian noise using  $a = 0.001$  and  $b = 0.3$  (Eq. (S10)), and then calculating  $\chi^2$  between the pseudo-experimental data and noiseless SAXS data from other conformational states of the pair (Fig. S3(b)). In the calculation, the unknown experimental parameters related to solvent density and intensity scaling were fixed. An example of the  $\chi^2$  plot on the 2D plane, which was calculated using the reference conformational state indicated by the red circle as the source of pseudo-experimental data is shown in Fig. S3(a). This plot indicated that the SAXS data depended on conformational changes along the first and second PC modes. However, a distinct region with consistently low  $\chi^2$  values, forming a banded shape, was also observed (Fig. S3(a) and S3(b)). Within this banded-shaped region, the distance between the centers of mass of the two domains,  $R_{\text{CM}}$ , remained relatively constant (Fig. S3(c)). These characteristics were observed for any conformational state within the 2D plane, indicating that the SAXS data for transferrin primarily depended on  $R_{\text{CM}}$ . Therefore,  $R_{\text{CM}}$  was utilized as the coordinate to describe the conformational motions of transferrin.

Furthermore, we delved into determining the optimal subset size for the coordinate  $R_{\text{CM}}$  in the reconstruction simulations. A key requirement for a subset was that all conformations within it yielded consistent SAXS data. Although smaller subset sizes satisfied this requirement, excessively small subset sizes increased the number of subsets, which was not ideal from a computational cost standpoint. Therefore, the subset size suitable for the reconstruction calculations was the largest among those that satisfied the aforementioned condition. Accordingly, we divided the coordinate  $R_{\text{CM}}$  into sufficiently small subsets of 0.05 Å and computed the  $\chi^2$  values for all subset pairs using the aforementioned procedure (Fig. S3(d)). The  $\chi^2$  values between the subsets separated by  $> 0.2$  Å

exceeded 1.5; therefore, we selected 0.2 Å as the subset size.

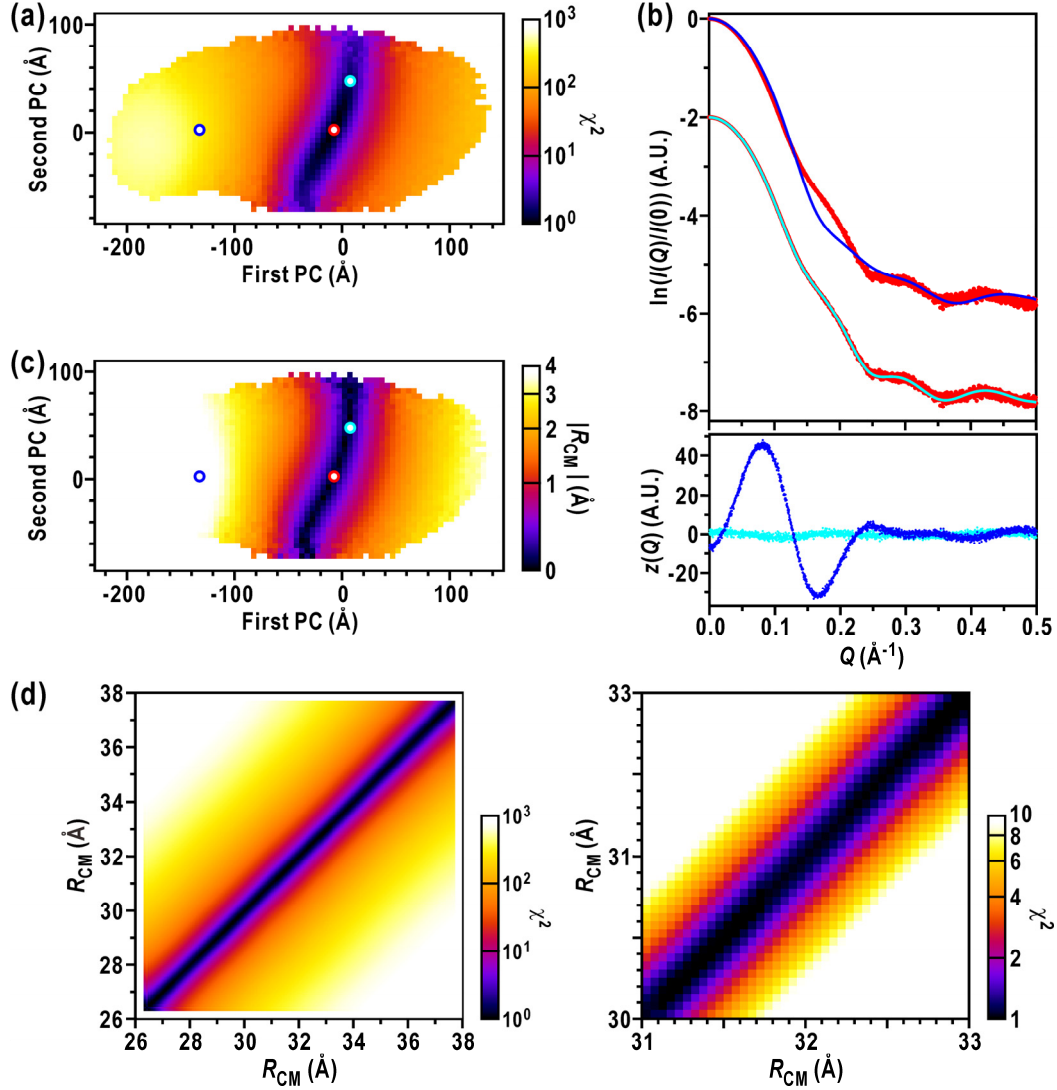


**FIG. S3.** Dependencies of the calculated SAXS data on conformational changes of transferrin. (a) Dependencies of  $\chi^2$  values on domain motions outlined by the first and second PC modes. The red circle indicates the conformation from which the pseudo-experimental SAXS data were generated. (b) Comparison of the pseudo-experimental SAXS data (red) with the data calculated from the two representative conformations, representing those indicated by the blue and cyan circles in (a). (c) Dependencies of the coordinate  $R_{CM}$  on the domain motions outlined by the first and second PC modes. The absolute value of the difference in  $R_{CM}$ ,  $|\Delta R_{CM}|$ , from the conformation utilized to generate pseudo-experimental SAXS data (red circle) was plotted by color. (d)  $\chi^2$  values between all pairs of conformations on  $R_{CM}$ , indicating the entire range (left panel) and magnified range (right panel) of  $R_{CM}$ .

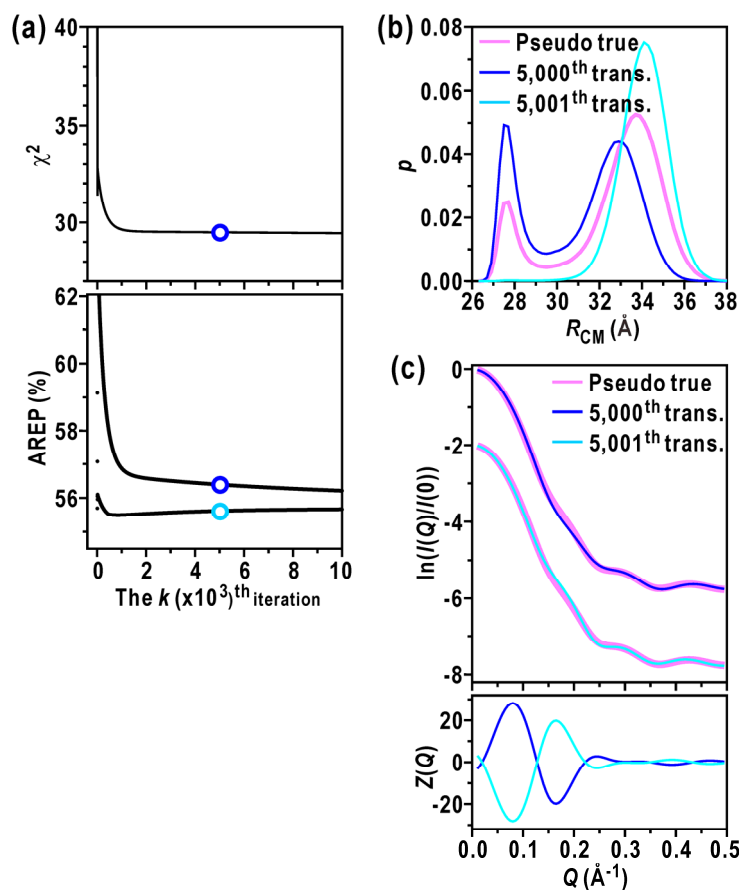


**FIG. S4.** Results of the reconstruction simulations when the large step size  $\delta$  of 0.025 was utilized. (a) Evolution of probability distribution monitored by  $\chi^2$  (upper) and AREP (lower). (b) Comparisons of the pseudo-true and estimated probability distributions. (c) Comparisons of the SAXS data.

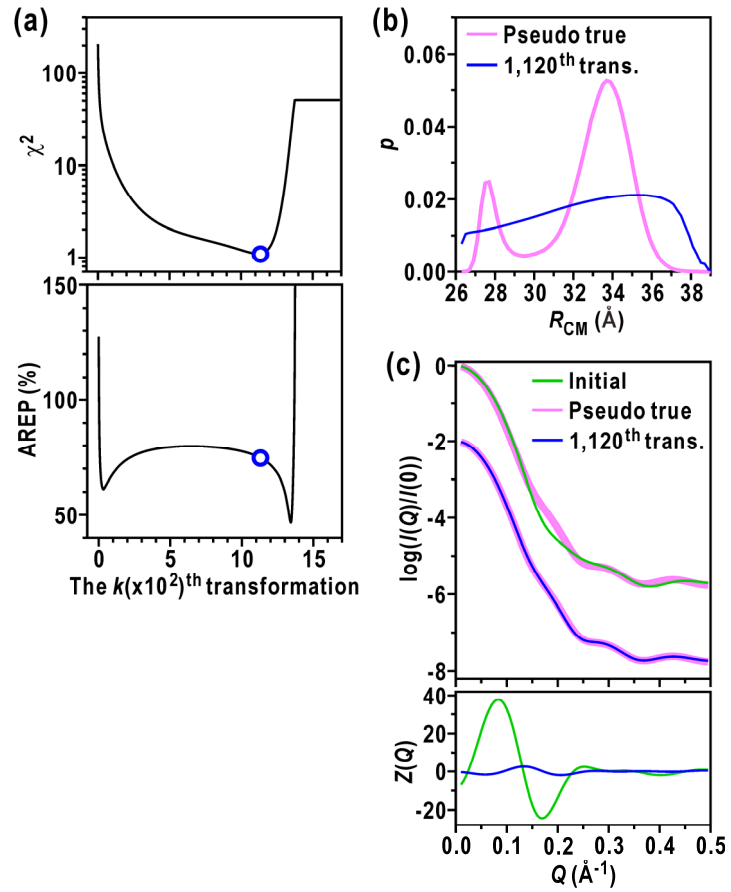


**FIG. S5.** Results of the reconstruction simulations when Eq. (19) was used. (a) Evolution of probability distribution was monitored by  $\chi^2$  (upper) and AREP (lower). (b) Comparisons of the pseudo-true and estimated probability distributions. (c) Comparisons of SAXS data.

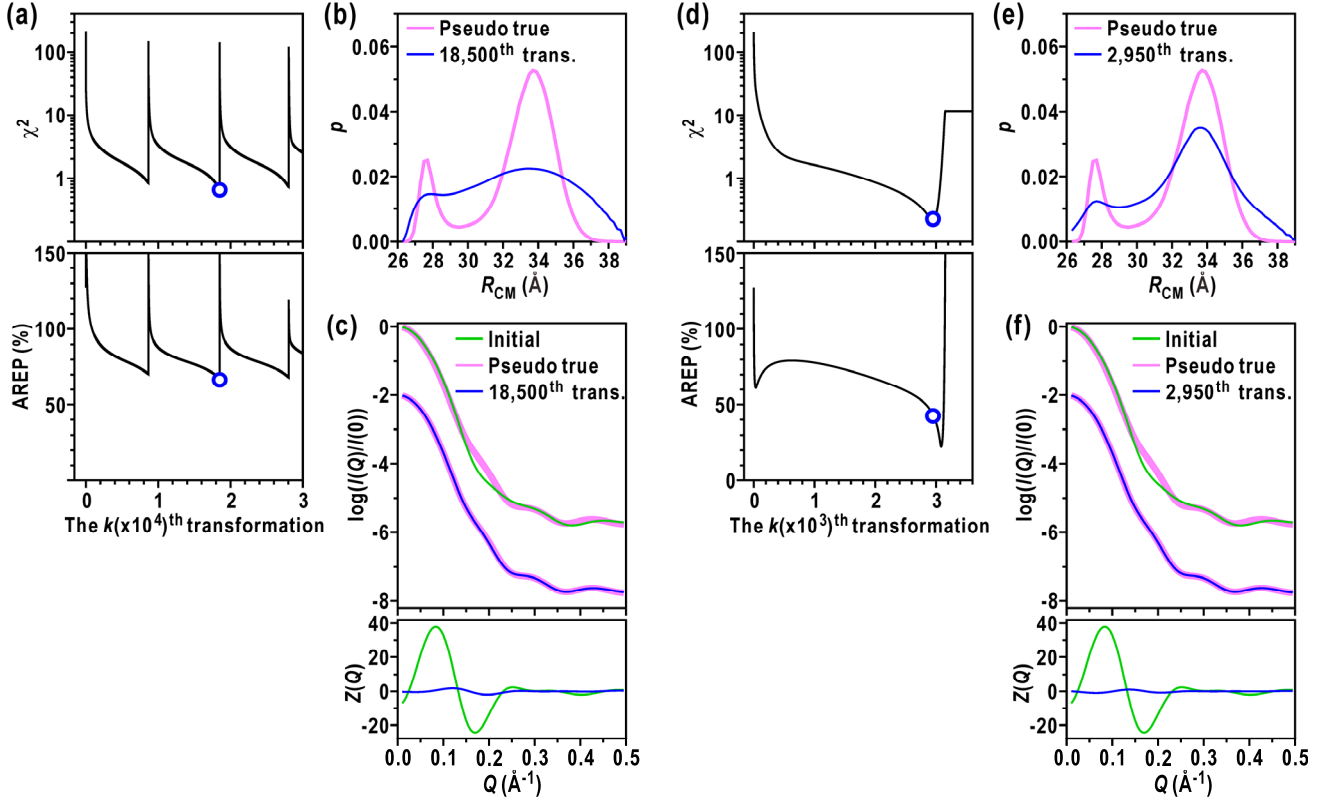


**FIG. S6.** Results of the reconstruction simulations using Eqs. (17) (a-c) and (18) (d-f) with the confidence factor value  $\kappa$ , which provided the optimal value of  $\chi^2$ . (a,d) Evolution of probability distribution was monitored by  $\chi^2$  (upper) and AREP (lower). (b,e) Comparisons of the pseudo-true and estimated probability distributions. (c,f) Comparisons of the SAXS data.

## REFERENCES

1. R. Salomon-Ferrer, D. A. Case and R. C. Walker, An overview of the Amber biomolecular simulation package, *WIREs Comput. Mol. Sci.* 3, 198 (2013).
2. L. Wang, K. A. McKierman, J. Gomes, K. A. Beauchamp, T. Head-Gordon, J. E. Rice, W. C. Swope, T. J. Martínez and V. S. Pande, Building a more predictive protein force field: a systematic and reproducible route to AMBER-FB15, *J. Phys. Chem. B* 121, 4023 (2017).
3. L. Wang, T. J. Martinez, V. S. Pande, Building force fields: an automatic, systematic and reproducible approach, *J. Phys. Chem. Lett.* 5, 1885 (2014).
4. P. D. Jeffrey, M. C. Bewley, R. T. A. MacGillivray, A. B. Mason, R. C. Woodworth and E. N. Baker, Ligand-induced conformational change in transferrins: crystal structure of open form of the N-terminal half-molecule of human Transferrin, *Biochemistry* 37, 13978 (1998).
5. U. Essmann, L. Perera, M. L. Berkowitz, T. Darden, H. Lee and L. G. Pedersen, Smooth particle mesh ewald method, *J. Chem. Phys.* 103, 8577 (1995).
6. J. P. Ryckaert, G. Ciccotti, H. J. C. Berendsen, Numerical integration of the Cartesian equations of motion of a system with constraints: molecular dynamics of *n*-alkanes, *J. Comput. Phys.* 23, 327 (1977).
7. H. Kenzaki, N. Koga, N. Hori, R. Kanada, W. Li, K. Okazaki, X. Q. Yao and S. Takada, CafeMol: a coarse-grained biomolecular simulator for simulating proteins at work, *J. Chem. Theory Comput.* 7, 1979 (2011).
8. R. T. A. MacGillivray, S. A. Moore, J. Chen, B. F. Anderson, H. Baker, Y. Luo, M. Bewley, C. A. Smith, M. E. P. Murphy, Y. Wang, A. B. Mason, R. C. Woodworth, G. D. Brayer and E. N. Baker, Two high-resolution crystal structures of the recombinant N-lobe of human transferrin reveal a structural change implicated in iron release, *Biochemistry* 37, 7919 (1998).
9. A. Kitao, F. Hirata and N. Gō, The effects of solvent on the conformation and the collective motions of protein: normal mode analysis and molecular dynamics simulations of melittin in water and in vacuum, *Chem. Phys.* 158, 447 (1991).
10. T. Ekimoto, Y. Kokabu, T. Oroguchi and M. Ikeguchi, Combination of coarse-grained molecular dynamics simulations and small-angle X-ray scattering experiments, *Biophys. Physicobiol.* 16, 377 (2019).
11. E. Valentini, A. G. Kikhney, G. Previtali, C. M. Jeffries and D. I. Svergun, SASBDB, a repository for biological small-angle scattering data, *Nucleic Acids Res.* 43, D357 (2015).
12. A. Guinier, and G. Fournet, *Small-angle scattering of X-rays*. (John Wiley and Sons, New York, 1955).